The Astrophysical Journal, 848:116 (14pp), 2017 October 20 https://doi.org/10.3847/1538-4357/aa8ad4

Can Substorm Particle Acceleration Be Applied to Solar Flares?

J. Birn[1,2], M. Battaglia[3], L. Fletcher[4], M. Hesse[5], and T. Neukirch[6]
[1] Space Science Institute, Boulder, CO 80301, USA; jbirn@lanl.gov
[2] Guest Scientist, Los Alamos National Laboratory, Los Alamos, NM 87545, USA
[3] Institute of 4D Technologies, School of Engineering, University of Applied Sciences and Arts Northwestern Switzerland, CH-5210 Windisch, Switzerland
[4] University of Glasgow, Scotland
[5] Birkeland Centre for Space Science, Department of Physics and Technology, University of Bergen, NO-5007 Bergen, Norway
[6] University of St. Andrews, Scotland
Received 2017 June 29; revised 2017 August 2; accepted 2017 August 30; published 2017 October 20

Abstract

Using test particle studies in the electromagnetic fields of three-dimensional magnetohydrodynamic (MHD) simulations of magnetic reconnection, we study the energization of charged particles in the context of the standard two-ribbon flare picture in analogy to the standard magnetospheric substorm paradigm. In particular, we investigate the effects of the collapsing field ("collapsing magnetic trap") below a reconnection site, which has been demonstrated to be the major acceleration mechanism that causes energetic particle acceleration and injections observed in Earth's magnetotail associated with substorms and other impulsive events. We contrast an initially force-free, high-shear field (low beta) with low and moderate shear, finite-pressure (high-beta) arcade structures, where beta represents the ratio between gas (plasma) and magnetic pressure. We demonstrate that the energization affects large numbers of particles, but the acceleration is modest in the presence of a significant shear field. Without incorporating loss mechanisms, the effect on particles at different energies is similar, akin to adiabatic heating, and thus is not a likely mechanism to generate a power-law tail onto a (heated or not heated) Maxwellian velocity distribution.

Key words: acceleration of particles – Sun: corona – Sun: flares – Sun: magnetic fields – Sun: particle emission

1. Introduction

It is generally accepted, and recently thoroughly confirmed (Aschwanden et al. 2017), that the energy released during solar eruptions is stored in the magnetic field before the eruption. Theoretical models of solar eruptions invariably include magnetic reconnection as a physical process, allowing the release of magnetic energy and its conversion into other forms of energy, such as bulk flow energy, thermal energy, and nonthermal particle energy with energies above ~10 keV. The nonthermal population may contribute as much as 50% or more of the total energy released in some flares (Miller et al. 1997; Emslie et al. 2005, 2012; Oka et al. 2015; Aschwanden et al. 2016). It is not clear how the inferred large number of energetic particles (more than 10^{36} per second in some flares, assuming the collisional thick target model for hard X-ray (HXR) production) is produced over very short timescales, as it would correspond roughly to all of the electrons in a coronal volume of $(10{,}000\ \mathrm{km})^3$ being accelerated at once. Therefore, the problem of solar flare particle acceleration is one of the most important and interesting problems in solar physics. Since similar phenomena are believed to occur in many other astrophysical objects throughout the universe, advancing our understanding of solar particle acceleration might also have implications for astrophysics in general.

An intriguing possibility for charged particle acceleration can be derived from the strong similarity between the standard two-ribbon flare model ("CSHKP" model, Carmichael 1964; Sturrock 1966; Hirayama 1974; Kopp & Pneuman 1976) and the standard near-Earth neutral line (NENL) model of magnetospheric substorms (e.g., McPherron et al. 1973; Hones 1977; Baker et al. 1996). In either case, reconnection in initially closed magnetic field lines (connected to the Sun or the Earth, respectively) is a key element in the energy release, leading to the ejection of plasma and magnetic flux outward and downward from the reconnection site. In the Earth's case, the collapse of the closed loops earthward of the reconnection site and the associated motional electric field have been identified as the major mechanism that causes acceleration of ions and electrons in the suprathermal (tens to hundreds of keV) energy range and their injection into the near magnetic tail and the inner magnetosphere, which are associated not only with substorms but also with smaller impulsive events (e.g., Birn et al. 2012, 2013, and references therein).

Energization in the collapsing and converging magnetic field ("collapsing magnetic trap") below a reconnection site has also been suggested as a possible particle acceleration mechanism in the flare scenario (e.g., Somov & Kosugi 1997; Karlicky & Kosugi 2004; Giuliani et al. 2005; Karlicky & Barta 2006). A number of investigations have addressed this mechanism, although mostly on the basis of analytical and test particle studies in assumed field models (e.g., Grady & Neukirch 2009; Grady et al. 2012; Eradat Oskoui & Neukirch 2014; Eradat Oskoui et al. 2014; Borissov et al. 2016). Karlicky & Barta (2007) used a two-dimensional MHD simulation of reconnection to study the test electron motion in the collapsing trap below the reconnection site and concluded it to be an efficient accelerator, particularly in relation to loop-top emissions. Assuming pre-energized source populations of 20 keV and 35 keV, they found further energizations up to 200 keV. A complication and constraint on possible acceleration mechanisms arises from the fact that bremsstrahlung emissions from target sources indicate a change of the electron population,

which is the source of the emissions with a power-law high-energy tail added to a pre-existing or heated Maxwellian (e.g., Lin & Krucker 2012).

In this study, we focus on the role of a collapsing trap, applying our simulation technique from substorms to the flare scenario. This technique consists of integrating test particle orbits in the time and space dependent magnetic and electric fields of an MHD simulation to investigate acceleration mechanisms and sources of accelerated particles. MHD simulations of reconnection in current sheets, flux ropes, or arcade structures with application to solar eruptions have been conducted by various authors in two spatial dimensions (e.g., Forbes & Priest 1983; Forbes et al. 1989; Inhester et al. 1992; Yokoyama & Shibata 2001) and three dimensions (e.g., Kusano 2002; Török & Kliem 2005; Ugai 2007; Amari et al. 2010; Török et al. 2013; Amari et al. 2014). Our MHD work goes beyond the current sheet and arcade models, particularly in using three-dimensional initial states and realistic low background pressure with low β (as low as 2×10^{-3}). In Section 2, we briefly discuss the chosen units, and in Section 3, we discuss the numerical approach involving MHD combined with test particle simulations, focusing here on electron orbits. In Section 4, we present MHD results important to understanding the background for the particle motion. Section 5 illustrates characteristic orbits and acceleration, Section 6 illustrates the effects of the chosen parameters on the location and magnitude of enhanced particle fluxes, Section 7 provides a global view of the regions of enhanced particle fluxes, and Section 8 demonstrates the characteristic source properties, in particular the source locations and energies of the accelerated particles. This is followed by a critical discussion in Section 9 and a summary in Section 10.

2. Basic Units

In the following equations, we use mostly dimensionless units, based on a characteristic magnetic field strength B_N, Alfvén velocity v_N, and scale length L_N. From these units we can derive, for instance, a density unit $n_N = (B_N/v_N)^2/(\mu_0 m_i)$, where m_i is the ion (here, the proton) mass, and an energy unit $W_N = \frac{1}{2} m_i v_N^2$. For illustration and a quantitative comparison with observed quantities, we will use two sets of units of the inflow region,

$$B_N = 100\ \mathrm{G} = 0.01\ \mathrm{T}$$
$$v_N = 5000\ \mathrm{km\ s^{-1}}$$
$$L_N = 10{,}000\ \mathrm{km}, \quad (1)$$

leading to a density unit $n_N = 1.9 \times 10^{15}\ \mathrm{m^{-3}}$, time unit $t_N = L_N/v_N = 2$ s, and energy unit $W_N = 4 \times 10^{-14}$ J = 130 keV, and

$$B_N = 100\ \mathrm{G} = 0.01\ \mathrm{T}$$
$$v_N = 1000\ \mathrm{km\ s^{-1}}$$
$$L_N = 10{,}000\ \mathrm{km}, \quad (2)$$

leading to a density unit $n_N = 4.9 \times 10^{16}\ \mathrm{m^{-3}}$, time unit $t_N = L_N/v_N = 10$ s, and energy unit $W_N = 5.2$ keV.

While there is some uncertainty and variability in the preflare parameters, these values are commensurate to those widely used in models of big flares. We use (mostly) standard international (SI) units with common notations and with k being the Boltzmann constant. Our coordinate system is chosen such that x is the coordinate perpendicular to the current sheet, y is in the direction of the main current, and z is the vertical direction.

3. Basic Approach

3.1. MHD Code

Our basic approach consists of an integration of the particle equations of motion in the suitably interpolated electric and magnetic fields of an MHD simulation. The one-fluid MHD code has been previously described in more detail (e.g., Birn et al. 1996, 2006). For the reader's convenience, we repeat some basics here. The code consists of an explicit, finite-difference, leapfrog scheme, based on two staggered meshes defined at alternate time steps. A nonlinear grid is used to increase the resolution in the regions of interest, such that about 1/2 of the grid points lie within the current sheet. A quasi-viscous term, which is similar to flux-corrected transport algorithms (e.g., Book et al. 1975), damps oscillations on the grid scale, reduces the divergence between the quantities on the two meshes, and increases numerical stability. This algorithm is not used on the magnetic field to avoid introducing artificial diffusion and reconnection. As for the equilibrium, gravity is neglected. We further neglect radiation and heat conduction, assuming an adiabatic law with a ratio of specific heats $\gamma = 5/3$, but include Ohmic heating.

The boundary conditions consist of solid, ideally conducting walls at each of the boundaries $z = 0$, $y = \pm y_{\max} = \pm 40$, and $x = \pm x_{\max} = \pm 10$, where all velocity components are set to zero (except for an initial driving phase, as discussed below). Von Neumann boundary conditions ($\partial/\partial n = 0$) are imposed on density, pressure, and the tangential magnetic field components, except at the top boundary $z = 60$, where an open outflow condition is assumed, such that B_x and B_y are convected with the plasma flow, while the normal magnetic field is held fixed. Line symmetry conditions are imposed around the z axis, such that only one half box $x \geqslant 0$ needed to be simulated.

For the orbit integration, the MHD fields were interpolated linearly in time. Drift orbit continuity, however, requires a cubic spline interpolation in space. To avoid artificial local maxima and minima, a monotonicity-conserving algorithm was employed (Hyman 1983).

3.2. Orbit Integration

The electron energies of interest approach, or may even exceed, the rest energy. Therefore, we use relativistic equations of motion, as described by Birn et al. (2004). The full motion of an electron with rest mass m_e and charge $-e$ is given by

$$\frac{D\boldsymbol{u}}{Dt} = -\frac{e}{m_e}\left(\boldsymbol{E} + \frac{1}{\gamma}\boldsymbol{u} \times \boldsymbol{B}\right), \quad (3)$$

where

$$\frac{D}{Dt} \equiv \frac{\partial}{\partial t} + \boldsymbol{w} \cdot \nabla. \quad (4)$$

Here, we have set $\boldsymbol{u} = \gamma \boldsymbol{w}$, where $\boldsymbol{w}$ is the electron velocity, and

$$\gamma = \frac{1}{\sqrt{1 - w^2/c^2}} = \sqrt{1 + u^2/c^2} \quad (5)$$

is the relativistic factor. The kinetic energy of the electron is then given by

$$W_{\rm kin} = (\gamma - 1) m_e c^2. \tag{6}$$

The drift of an electron with rest mass m_e, (relativistic) magnetic moment μ_r, and charge $q = -e$ is governed by (e.g., Northrop 1963; Birn et al. 2004)

$$\boldsymbol{v}_d = \boldsymbol{v}_E - \frac{\mu_r}{\gamma e}\frac{\boldsymbol{B}\times\nabla B}{B^2} - \frac{m_e\gamma v_\parallel}{e}\frac{\boldsymbol{B}}{B^2}\times\frac{d\boldsymbol{b}}{dt} - \frac{m_e}{e}\frac{\boldsymbol{B}}{B^2}\times\frac{d\gamma\boldsymbol{v}_E}{dt} \tag{7}$$

and

$$\frac{du_\parallel}{dt} = -\frac{e}{m_e}E_\parallel - \frac{\mu_r}{\gamma m_e}\frac{\partial B}{\partial s} + (\boldsymbol{u}_E + \boldsymbol{u}_{\nabla B})\cdot\frac{d\boldsymbol{b}}{dt}, \tag{8}$$

where $\boldsymbol{b} \equiv \boldsymbol{B}/B$,

$$\boldsymbol{v}_E = \frac{\boldsymbol{E}\times\boldsymbol{B}}{B^2}, \tag{9}$$

and

$$\frac{d}{dt} \equiv \frac{\partial}{\partial t} + (\boldsymbol{v}_\parallel + \boldsymbol{v}_d)\cdot\nabla \tag{10}$$

is the time derivative along the drift orbit. The relativistic magnetic moment μ_r is defined by

$$\mu_r = \frac{p_\perp^2}{2m_e B}, \tag{11}$$

where $p_\perp = m_e\gamma w_\perp = m_e u_\perp$ is the perpendicular relativistic momentum associated with the gyration speed $w_\perp$. The kinetic energy is then given by (6) with

$$\gamma = \sqrt{1 + (u_\parallel^2 + 2\mu_r B/m_e + u_E^2)/c^2}, \tag{12}$$

where $u_\parallel = \gamma v_\parallel$ and $\boldsymbol{u}_E = \gamma\boldsymbol{v}_E$. We note that we do not distinguish between the parallel speed of the particle and that of the gyrocenter. The drift contributions are neglected in the energy expression (12) because these contributions are even smaller than the $\boldsymbol{E}\times\boldsymbol{B}$ drift contribution in comparison to those of the gyromotion and the parallel motion.

Based on dimensionless units and neglect of the inertia contributions, the electron drift equations used here are given by (Birn et al. 2004; correcting a typo in their Equation (15))

$$\hat{\boldsymbol{v}}_d = \hat{\boldsymbol{v}}_E - \frac{\epsilon\hat{\mu}}{2\gamma}\frac{\hat{\boldsymbol{B}}\times\nabla\hat{B}}{\hat{B}^2} - \frac{\epsilon\,\hat{u}_\parallel^2}{\gamma}\frac{\hat{\boldsymbol{B}}}{\hat{B}^2}\times\frac{\partial\boldsymbol{b}}{\partial\hat{s}} \tag{13}$$

$$\frac{d\hat{u}_\parallel}{d\hat{t}} = -\frac{1}{\epsilon\sigma}\hat{E}_\parallel - \frac{\hat{\mu}}{2\sigma\gamma}\frac{\partial\hat{B}}{\partial\hat{s}} + \frac{\hat{u}_\parallel}{\gamma}(\hat{\boldsymbol{u}}_E + \hat{\boldsymbol{u}}_{\nabla B})\cdot\frac{\partial\boldsymbol{b}}{\partial\hat{s}}, \tag{14}$$

where

$$\epsilon = \frac{1}{\omega_{ci}t_N} = \frac{m_i}{eB_N t_N} \tag{15}$$

and

$$\sigma = \sqrt{m_e/m_i}, \tag{16}$$

and the symbol $\hat{}$ is used to denote dimensionless quantities with $\hat{\boldsymbol{v}}_E = \boldsymbol{v}_E/v_N$, $\hat{\boldsymbol{v}}_{\nabla B} = \boldsymbol{v}_{\nabla B}/v_N$, but $\hat{\boldsymbol{u}}_\parallel = \boldsymbol{u}_\parallel/v_{ce}$, where $v_{ce} = v_N/\sigma$, and m_i is the ion (here, the proton) mass. We note the different scaling of the velocity contributions, which is used to keep the normalized quantities in the range of unity, as $v_\parallel$ and the gyromotion speed in the energy range of interest are typically several orders of magnitude larger than the drift speeds. Also, only the leading term of $d\boldsymbol{b}/dt \approx 1/(\sigma\gamma)\hat{u}_\parallel\partial\boldsymbol{b}/\partial\hat{s}$ is retained. The (normalized) kinetic energy of an electron in the drift approximation is then given by

$$\hat{W} = 2(\gamma - 1)c^2/v_{ce}^2, \tag{17}$$

where

$$\gamma = \sqrt{1 + (v_{ce}^2/c^2)(\hat{u}_\parallel^2 + \hat{\mu}\hat{B})}. \tag{18}$$

Electron orbits were mostly integrated using the gyro-drift approximation based on the conservation of the magnetic moment μ. However, this approximation breaks down in regions of low magnetic field strength, which are found in the high-beta, low-shear configurations. In that case, the integration was switched to full orbit integration, (3). The switch between the two types of orbit integrations was based on the magnitude of an adiabatically parameter, representing the square root of the ratio between field line curvature radius and gyoradius (Büchner & Zelenyi 1989; Birn et al. 2004).

3.3. Boundary Conditions on Particle Orbits

Particle orbits were integrated backward in time until they reached the initial state of the MHD simulation, or one of the top (z), or side boundaries in x or y. Particle fluxes at the final time could then be obtained from phase space density (PSD) distributions $f(\boldsymbol{r}, \boldsymbol{v}, t)$ imposed at those source locations, using Liouville's theorem of the conservation of f along a phase space trajectory in the absence of collisions. Collisions are expected to reduce the effects of the acceleration (e.g., Hamilton et al. 2005). Our collisionless approximation is therefore expected to provide upper limits on the acceleration from the collapse (see also the discussion section.) The source distributions were chosen as either Maxwellian or kappa distributions (e.g., Vasyliunas 1968; Oka et al. 2013), defined by

$$f_{0\kappa} \propto \left(1 + \frac{v^2}{\kappa v_0^2}\right)^{-\kappa-1}. \tag{19}$$

The kappa distribution includes the transition to a power-law tail at high energies, accounting for some unspecified prior acceleration. However, when considering fluxes at a fixed final energy W, we simply used the energy gain $\Delta W = W - W_0$ as a proxy for the fluxes. For a Maxwellian distribution, this measure is proportional to the logarithm of the particle flux or PSD as follows:

$$f(W, t) = f_{0M}(W_0, t_0) = C\exp(-W_0/kT_0) \tag{20}$$

such that

$$\log f = \log f_{0M} = \log C - \frac{W_0}{kT_0}\log e = \text{const} + \frac{\log e}{kT_0}\Delta W. \tag{21}$$

At the bottom boundary $z = 0$, we simply used a reflection of the particle orbit, reversing the parallel velocity but conserving the gyrocenter location and magnetic moment. While this procedure can be justified in the magnetotail case from the particle motion into the much larger Earth's dipole

field, it is more questionable in the solar case. We will discuss it and the possible consequences in more detail in Section 9.

3.4. Parallel Electric Field

In the simple CSHKP flare scenario, reconnection happens at a single (generalized) x-line or separator. The presence of a parallel electric field, identifying reconnection in general configurations (e.g., Schindler et al. 1988), would be confined to a narrow, nonideal region around the separator. In the collisionless limit, the dimension of this region perpendicular to the magnetic field is of the order of an ion inertial length (e.g., Drake & Shay 2007; Hesse 2007), which can be estimated to be a few meters for the parameters in Equations (1)–(2). Assuming Spitzer resistivity, one arrives at similar lengths. This is significantly smaller than the $\boldsymbol{E} \times \boldsymbol{B}$ drift distance during a particle bounce, which can be estimated at 10–100 km, using a (normalized) reconnection rate of 0.01. Thus, only relatively few particles are expected to experience the acceleration from the parallel electric field, which is consistent with conclusions from x-line acceleration models (e.g., Hannah & Fletcher 2006), and they will presumably reach higher energies that are out of the range of our interest. In contrast, due to numerical restrictions of the MHD simulations, the spread of the resistive electric field, $\eta j_{\parallel}$, is much wider than what is realistic and would have anomalously large effects on the particle motion. Consequently, in order to isolate the effects of the acceleration in the collapsing reconnected fields, it seems better to ignore the parallel electric field completely.

3.5. Hall Parameter

Equations (13) and (14) contain the small parameter ϵ that is defined by Equations (15), which can also be expressed as $\epsilon = d_i/L_N$, where d_i is the ion inertial length. This parameter is often denoted as the Hall parameter. In the geomagnetic tail, it is of the order of $1/10$ to $1/50$. Based on the numbers in Equations (1)–(2), it is of the order of 10^{-6} to 10^{-7} in the solar corona, which makes it numerically difficult to track the effects of the gradient/curvature drifts in the orbit integrations. However, the gain (or the loss) of electron energy from drift opposite to (or parallel to) the direction of the electric field is given by

$$\Delta W = -e \int \boldsymbol{E} \cdot d\boldsymbol{s} = -e \int \boldsymbol{E} \cdot \boldsymbol{v}_d \, dt. \tag{22}$$

If Equation (22) is normalized, then it contains a factor $1/\epsilon$, which compensates the factor ϵ in the drift speeds in Equation (13). Since the $\boldsymbol{E} \times \boldsymbol{B}$ drift does not contribute to Equation (22), the energy gain or loss hence becomes independent of ϵ. Due to the neglect of the parallel electric field, Equation (14) also becomes independent of ϵ. It thus seems justified to choose the more manageable value of

$$\epsilon = 0.005 \tag{23}$$

for our orbit integrations.

3.6. Relativistic Parameter

Apart from the fixed ion/electron mass ratio, the equations in Section 3.2 contain another dimensionless parameter. This parameter is contained, for instance, in Equation (18) as

$$\xi = \frac{v_{ce}^2}{c^2} = 2\frac{W_N}{m_e c^2}. \tag{24}$$

The parameter ξ describes how relativistic the chosen unit energy is. When ξ is small, then the equations become nonrelativistic. We obtain $\xi = 1/1.96 = 0.51$ for the parameter set in Equation (1), and $\xi = 1/48.9 = 0.02$ for the parameter set in Equation (2). It turns out, however, that the results are only weakly affected by the value of ξ, even when ξ approaches unity.

4. MHD Simulations

Our initial states are described by Birn et al. (2009) and are partially repeated here. These configurations consist of a stretched current sheet field, which is expected below a departing coronal mass ejection, changing farther below toward a 3D dipole magnetic field with a location of the dipole below the photospheric surface. Since the simple superposition leads to fields that are no longer in an exact force balance, a relaxation method (Hesse & Birn 1993) was used to obtain force-balanced equilibria before starting the simulation of the dynamic evolution.

Three types of arcade configurations were considered; the two extreme cases are illustrated in Figures 1(a) and (b). One is initially force-free (Figure 1(a)), which means that the current density vector is aligned with the magnetic field. In this type of configuration, the pressure of the magnetic field that reverses across the current sheet, B_z, is balanced by the magnetic pressure of the component in the main current direction, B_y, which is frequently called the "guide field" or the shear field. In the other case (Figure 1(b)), the guide field is assumed to be small or zero, and the outside magnetic pressure is balanced by the plasma pressure inside the current sheet. In addition to the cases illustrated in Figure 1, we have considered a case that includes both finite shear and finite pressure in the current sheet. In the following, we refer to these cases as high shear (HS), low shear (LS), and medium shear (MS), respectively. In all of the cases, a small uniform background plasma pressure of $\sim$1% of the total pressure was added. While the force-free and the nonforce-free initial states are distinguished by low and high β in the current sheet, the background has a low $\beta \approx 0.01$ or even $\beta \approx 0.002$. Such values appear reasonable above solar active regions (e.g., Gary 2001).

The simulations include a slow phase of the current intensification prior to the initiation of reconnection, resulting from a slow converging motion at the bottom boundary $z = 0$ in the x direction toward the field reversal near $x = 0$. This motion, with a maximum amplitude at $y = 0$, is gradually turned on and off, as described in detail by Birn et al. (2009). During this phase, the resistivity is set to zero, allowing for an additional current to build or concentrate under the action of the slow driving.

As described by Birn et al. (2009), the following eruptive phase is initiated by imposing a localized finite resistivity, which is centered near the peak of the current intensification. This resistivity, in combination with the current intensification from the driven phase, leads to the onset of reconnection. The subsequent evolution of the magnetic field is illustrated by Figure 1, panels (c) and (d), for the high-shear and the low-shear case, respectively (modified after Birn et al. (2009)). Both

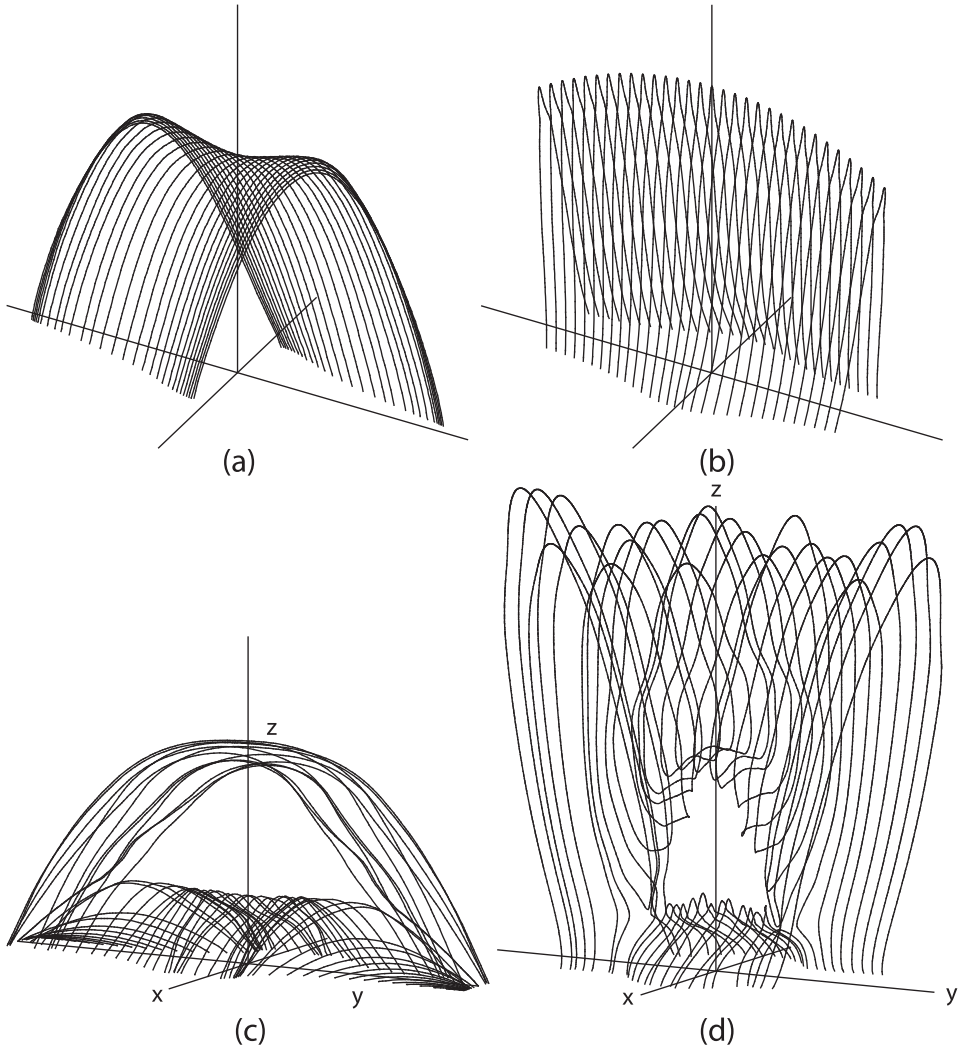

Figure 1. Perspective view of magnetic field lines during the plasmoid ejection (after Birn et al. 2009). Panels (a) and (c) show the high-shear (initially force-free) case. Panels (b) and (d) show the low-shear (high-beta) case.

cases show the ejection as a more (Figure 1(d)) or less (Figure 1(c)) tightly wound flux rope and as a collapse of the field underneath the reconnection site. This collapsing region is the region of interest for the present particle study.

Concerning the particle acceleration, our particular interest is the structure and evolution of the electric field, which, outside of the reconnection site, is given by the ideal field $-\boldsymbol{v} \times \boldsymbol{B}$. Figure 2 shows the horizontal component of the electric field E_x for the high-shear case at five successive times in the y, z and x, z planes. A positive (or negative) E_x indicates a downward (or upward) flow. The white circles indicate plasma elements traced with the flow, and the red and blue lines are projections of the field lines crossing the location of the elements. Figure 2 illustrates that an early, roughly two-dimensional reconnection structure splits up into two reconnection sites. A possible cause may be the development of an interchange type of mode. The plasma element on the red field line is initially on an open field line that undergoes a reconnection. This element experiences strong downward acceleration. In contrast, the element on the blue field lines is initially already on a closed field line below the reconnection site. It undergoes only a moderate downward acceleration. The downward flow stops around $t = 115$, and the plasma elements and field lines indicate an up and down bouncing for a few periods.

In a similar fashion, Figure 3 shows the horizontal component E_y for the medium-shear case at three successive times in the y, z and x, z planes. A positive (or negative) E_y also corresponds to a downward (or upward) flow. The white circles again indicate a plasma element traced with the flow, and the blue lines are projections of the field lines crossing the location of the element. In contrast to the high-shear case (Figure 2), the downward flow remains peaked near the center, although it splits up into several sites at later times. This is similar to the low-shear case, which has been studied more extensively in the context of the terrestrian magnetotail (e.g., Birn et al. 2013, 2014) and is therefore not shown here.

5. Typical Orbits and Acceleration

Following the procedure described in Section 3, we have traced particle orbits backward in time from various locations in space, selecting fixed final energies, times, and pitch angles. As discussed in Section 3.3, the energy gain is used as a proxy of the flux increases. Figure 4 illustrates the typical orbits of accelerated particles superposed on the color-coded display of

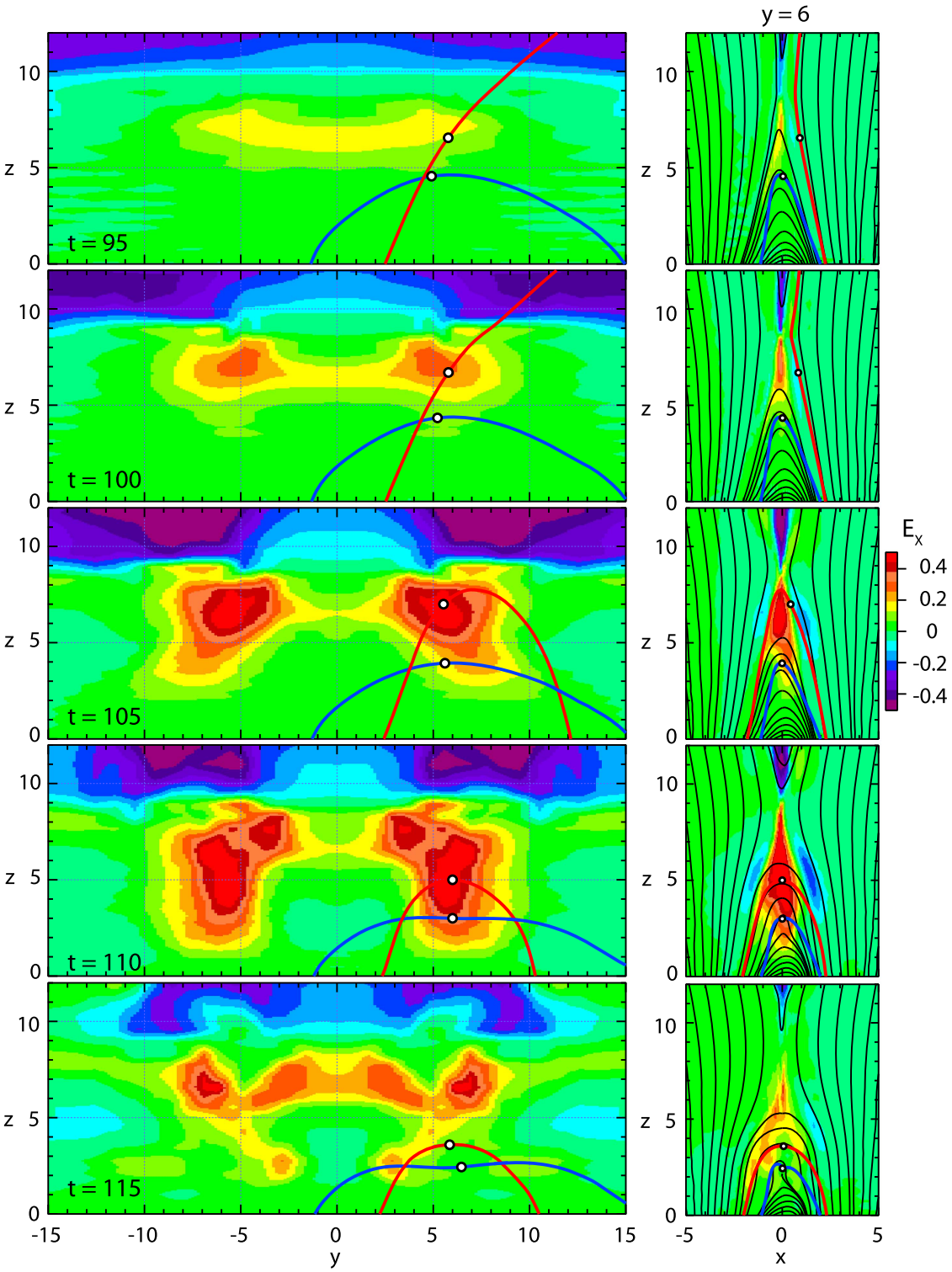

Figure 2. Horizontal electric field component E_x in the y, z and x, z planes for the high-shear case, indicating the downward (and upward) flow from the reconnection site. The white circles indicate plasma elements traced with the flow, and the red and blue lines are projections of the field lines crossing the location of the elements.

the relative energy gain in the x, z plane, which were obtained at the final times. The times were chosen to coincide with the primary peak of the downward energy flux in the MHD simulations, which are (a-c) $t = 110$ for the high-shear, (d) $t = 110$ for the medium-shear, and (e) $t = 130$ for the low-shear case. All particles had a final energy of $W = 31.6$ keV. The (normalized) particle energies corresponding to the orbits in Figure 4 are shown in Figure 5 together with the perpendicular and parallel energies at the $x = 0$ crossings, defined by

$$\hat{W}_{\parallel} = \hat{u}_{\parallel}^2, \tag{25}$$

$$\hat{W}_{\perp} = \hat{\mu}\hat{B}. \tag{26}$$

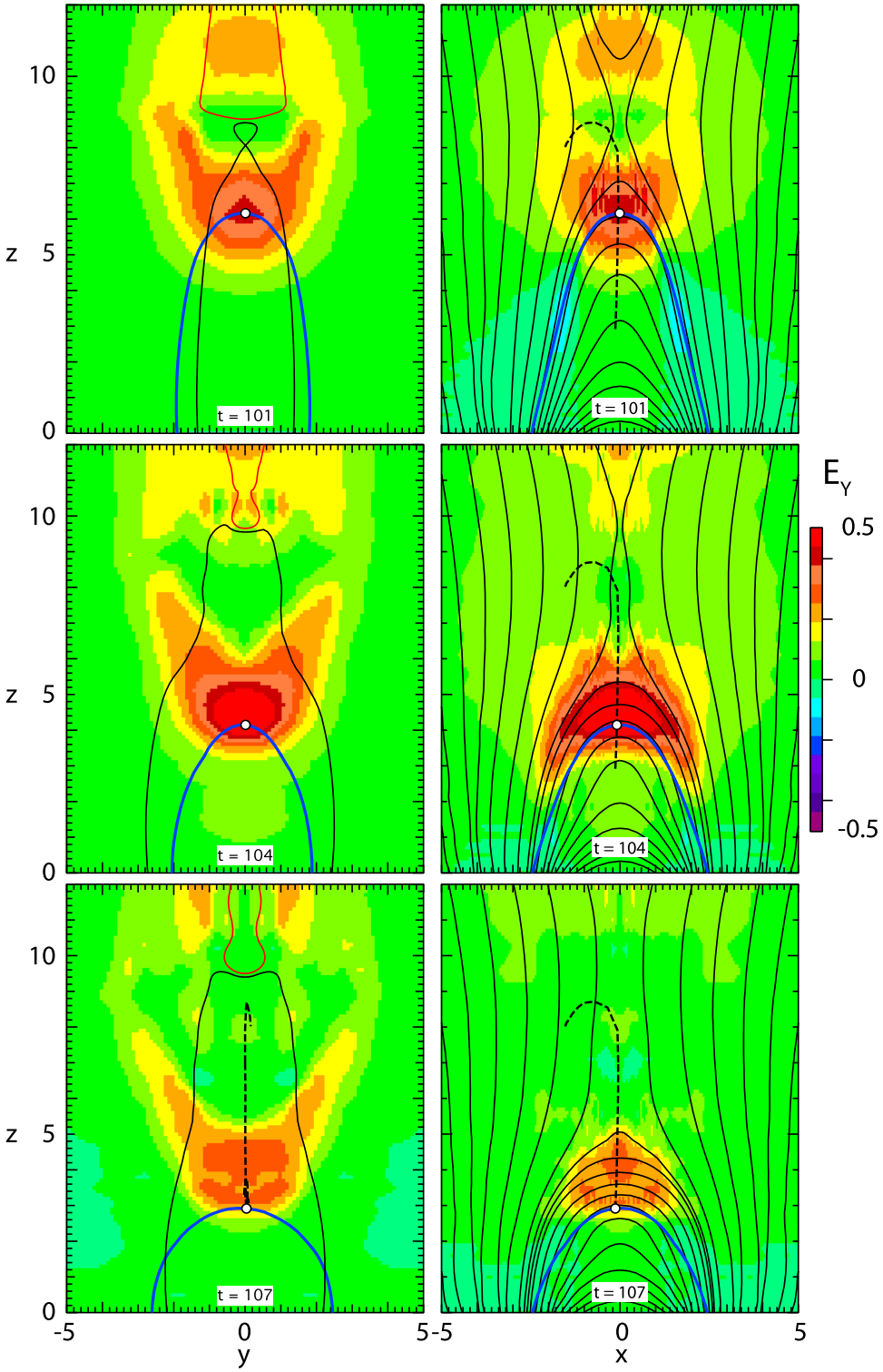

Figure 3. Horizontal electric field component E_y in the y, z and x, z planes for the medium-shear initial case, indicating the downward (and upward) flow from the reconnection site. The white circles indicate again a plasma element traced with the flow, the dashed line shows the path of this element toward and out of the reconnection site, and the blue lines are projections of the field lines crossing the location of the element.

We note that, in the relativistic regime, the total energy is not simply the sum of Equations (25) and (26), but follows from Equations (17) and (18).

The particles typically enter the collapsing field from outside on field lines that undergo reconnection. The low pitch angle particle (Figures 4(a) and 5(a)) reaches the bottom boundary ($z = 0$) and becomes reflected several times. It gains parallel energy (red dots in Figure 5(a)) at each crossing of the $x = 0$ plane at the loop tops. The 60° (final) pitch angle particles in both the high-shear and low-shear cases (Figures 4(b) and (e), and Figures 5(b) and (e)) originally start with nearly equal amounts of parallel and perpendicular energy, but gain energy only in the perpendicular component (blue dots), which happens again near the loop tops at the crossings of the $x = 0$

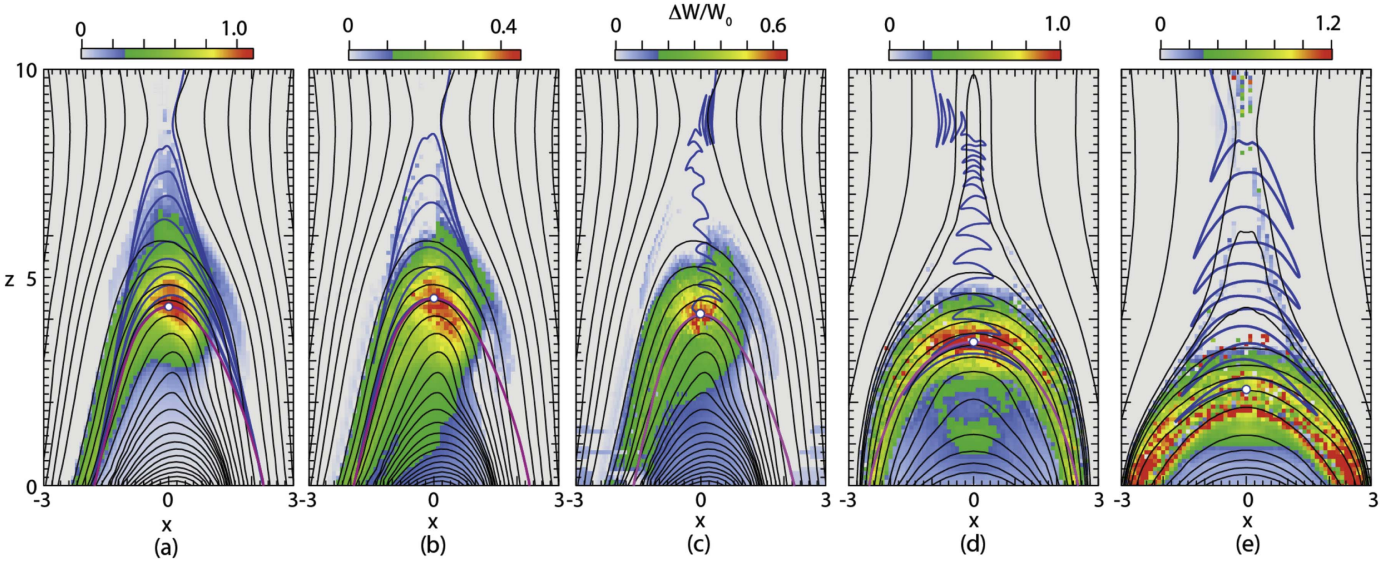

Figure 4. Typical orbits of accelerated particles projected into the x,z plane. The orbits are superposed on snapshots of the 31.6 keV particle fluxes (measured by the relative energy gain) in the $y = 0$ plane. Panels (a)–(c) are for the high-shear, (d) is for the medium-shear, and (e) is for the low-shear case. The relativistic parameter was $\xi = 0.51$ in all cases, the final energy was $W = 31.6$ keV, and the final pitch angle at $x = y = 0$ $\alpha = 5°$ for (a), $\alpha = 60°$ for (b) and (e), and $\alpha = 85°$ for (c) and (d). The final locations, indicated by the white dots, were chosen to be central within the region of the enhanced flux. Black contours show the magnetic field in the x, z plane. In the low-shear case only, these lines are close to the actual field lines; the projections of field lines crossing the final point of the chosen orbits are shown in purple.

plane. Particles with pitch angles close to 90° (Figures 4(c) and (d)) commonly become trapped in the local minimum B field in the inflow region, where they lose some energy via the inverse betatron effect due to the decreasing field magnitude (Figures 5(c), (d)). In the outflow region they also gain energy in a stepwise fashion at the crossings of the $x = 0$ plane, i.e., the loop top. One might consider attributing this to the shortening of the flux tube or slingshot effect of the collapsing field (i.e., the Fermi acceleration of type A or B; Northrop 1963), causing an increase in the parallel energy. However, Figure 5(a) demonstrates that this is only the case for small pitch angles. However, these orbits are reflected at the bottom boundary ($z = 0$). This assumption is presumably unrealistic, as discussed in Section 9.

It is also noteworthy that none of the orbits illustrated in Figure 4 have come close enough to the generalized x-line or the separator to have crossed the presumed region of the parallel electric field (within the estimated ion inertial length or resistive scale). Thus, pre-acceleration by the direct electric field is probably not an important factor unless this region were greatly extended, for instance, through turbulent effects.

The stepwise energy gain, as illustrated in Figure 5, can be interpreted in two ways. This becomes obvious from the energy equations (see Giuliani et al. 2005; Grady et al. 2012), which, for simplicity, we write in its nonrelativistic form, which is derived from Equations (7) and (8) with neglect of the inertia term

$$\frac{d}{dt}\frac{m_e}{2}v_\perp^2 = \mu\frac{dB}{dt} = \mu\left(\frac{\partial B}{\partial t} + v_\parallel\frac{\partial B}{\partial s} + \boldsymbol{v}_E\cdot\nabla B\right) \tag{27}$$

$$\frac{d}{dt}\frac{m_e}{2}v_\parallel^2 = -ev_\parallel E_\parallel - \mu v_\parallel\frac{\partial B}{\partial s} + m_e v_\parallel \boldsymbol{v}_E\cdot\frac{d\boldsymbol{b}}{dt}. \tag{28}$$

The parallel electric field term is included in Equation (28) for completeness; although, it is disregarded in our orbit calculations, as discussed in Section 3.4. The first and last terms on the rhs of Equation (27) describe the betatron effect from the increasing (or decreasing) magnetic field strength or the $\boldsymbol{E}\times\boldsymbol{B}$ drift motion into the spatially increasing (or decreasing) magnetic field. Similarly, the last term in Equation (28) describes the gain (or loss) from the motion in a curved field, which is the first-order Fermi acceleration (type B; Northrop 1963). However, these last terms can also be re-written as

$$\mu\boldsymbol{v}_E\cdot\nabla B = -e\boldsymbol{v}_{\nabla B}\cdot\boldsymbol{E} \tag{29}$$

$$m_e v_\parallel \boldsymbol{v}_E\cdot\frac{d\boldsymbol{b}}{dt} = -e\boldsymbol{v}_c\cdot\boldsymbol{E}, \tag{30}$$

where $\boldsymbol{v}_{\nabla B}$ and $\boldsymbol{v}_c$ are the gradient and curvature drifts, as defined in Equation (7). Thus, the betatron and Fermi acceleration of the electrons in the collapsing field are equivalent to the gradient B and curvature drift components, respectively, antiparallel to the electric field (see, Northrop 1963; Birn et al. 2013). These terms dominate the acceleration. It occurs at the loop tops because both the $\boldsymbol{E}\times\boldsymbol{B}$ drift and the field gradients are largest there.

6. Parameter Effects

Choosing the high-shear, initially force-free case as an example, we have explored the influence of various parameters on the amount and location of particle acceleration. Figure 6 provides a comparison of the flux enhancements for $t = 110$ at $z = 1$, which is slightly above the photospheric boundary, for different energies, pitch angles, and relativistic parameters ξ (representing the ratio of the characteristic energy to the electron rest energy). Panels (a)–(d) of Figure 6 show the relative energy gains, as a proxy of the flux enhancement, for different parameters indicated in the margin, while panels (e)–(g) show MHD quantities that might be related to the energetic particle fluxes: downward Poynting flux S_z, enthalpy flux H_z, and temperature T.

A comparison between panels (a) and (b) of Figure 6 shows that the location of the flux enhancements and the relative

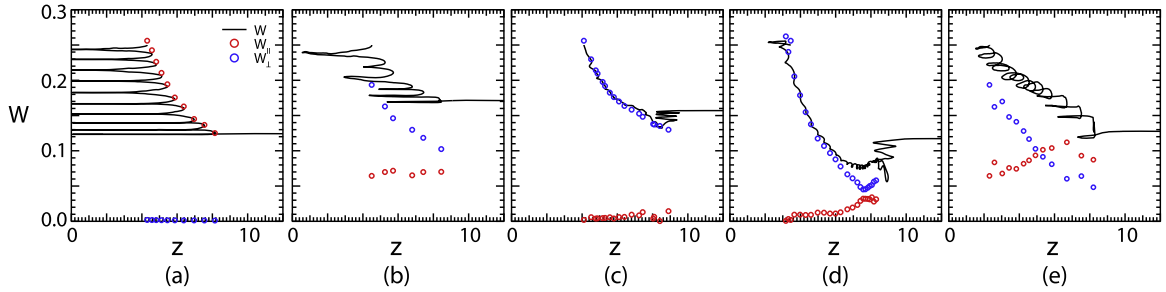

Figure 5. Energy as function of z for the orbits in Figure 4. The red and blue circles show parallel and perpendicular energies at the crossing of the $x = 0$ plane. In each case, the start point is to the right and the end point is at the top.

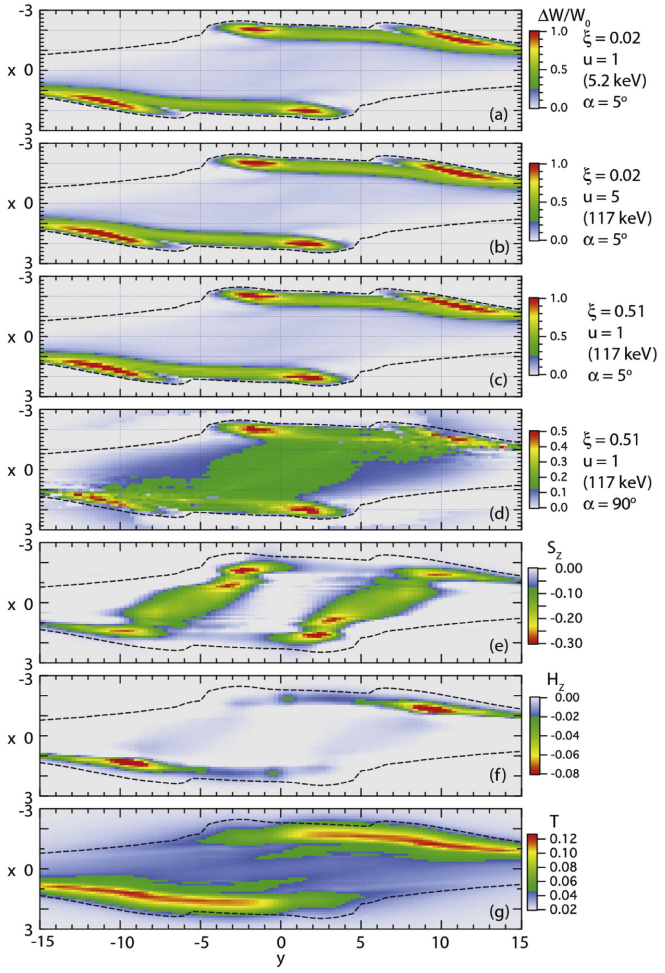

Figure 6. Particle fluxes and MHD properties at $z = 1$ for the high-shear case at $t = 110$. Panels (a)–(d): particle energy gains for different relativistic parameters ξ, energies W, and pitch angles α, as indicated in the margin; panels (e)–(g): the downward Poynting flux S_z, enthalpy flux H_z, and temperature T from the MHD simulation.

energy gain is about the same for different final energies. A comparison between panels (a) and (c) shows again identical locations, but a slightly smaller relative energy gain in the more relativistic case $\xi = 0.51$, which is consistent with the conclusions of Eradat Oskoui & Neukirch (2014). Finally, a comparison between panels (c) and (d) again shows no change in the location but a lower energy gain for 90° pitch angle than for 5° pitch angle. Since this result strongly depends on our assumed reflective boundary condition at $z = 0$, it will be critically discussed in Section 9. In summary, the locations of the enhanced fluxes show no significant influence of the energy, pitch angle, or relativistic parameter. This is obviously related to the fact that the particle gradient and curvature drifts, which are affected by these parameters, are very small compared to the $\boldsymbol{E} \times \boldsymbol{B}$ drift and the field-aligned motion, such that the particles stay close to the same field line and therefore undergo similar histories. The relative energy gains depend somewhat on the pitch angle and are generally slightly smaller in the more relativistic regime (a large ξ).

The comparison between the particle results (Figures 6 (a)–(d)) and the MHD quantities (Figures 6(e)–(g)) shows that the particle flux enhancements closely (but not exactly) coincide with the enhancements of the downward Poynting and the enthalpy flux. This is probably related to the fact that the locations of enhanced particle fluxes in the test particle simulations are insensitive to the particle energy. In contrast, the MHD temperature enhancement occurs over two more extended ribbons. However, the peak particle fluxes are embedded in somewhat less enhanced fluxes that more closely resemble the MHD ribbons of an increased temperature.

7. Spatial Overview of Simulated Particle Fluxes

A more comprehensive view of the enhanced particle fluxes in different planes is provided in Figures 7 and 8, showing perspective views of the simulated particle fluxes in the x, y and y, z planes with a few field lines connecting the regions of the enhanced flux (blue lines). Figure 7 is obtained in the high-shear field for particles of a unit velocity with a pitch angle of $\alpha = 5°$, both at $z = 0$ and $x = 0$ in the weakly relativistic case $\xi = 0.02$ (the parameter set in Equation (2)) at a time $t = 110$ when the MHD simulation indicated a peak in the downward enthalpy and the Poynting flux (Birn et al. 2009). Although a pitch angle of 5° at $z = 0$ corresponds to a smaller value at $x = 0$, the fluxes at the proper pitch angles should be very similar, as the locations of the enhanced fluxes are insensitive to the pitch angle. The color shows the energy gain. Since the final energy is $\hat{W} \approx v^2 = 1$, this indicates that the peak fluxes result from particles that have doubled their energy. Through their bounce motions, they fill two flux bundles, which are related to the two active reconnection sites and the downflows indicated in Figure 2. The black solid and dashed lines indicate the separatrix. The orange line in Figure 7 shows a sample orbit of an electron contributing to the enhanced fluxes similar to the one in Figure 4(a).

The particle fluxes enhancements in the medium- and low-shear cases are similar to those in the high-shear case, except that they are associated with just a single acceleration site. This is shown in Figure 8 for the medium- and low-shear cases with $\xi = 0.51$ and $\xi = 0.02$, respectively. Again, the blue lines are

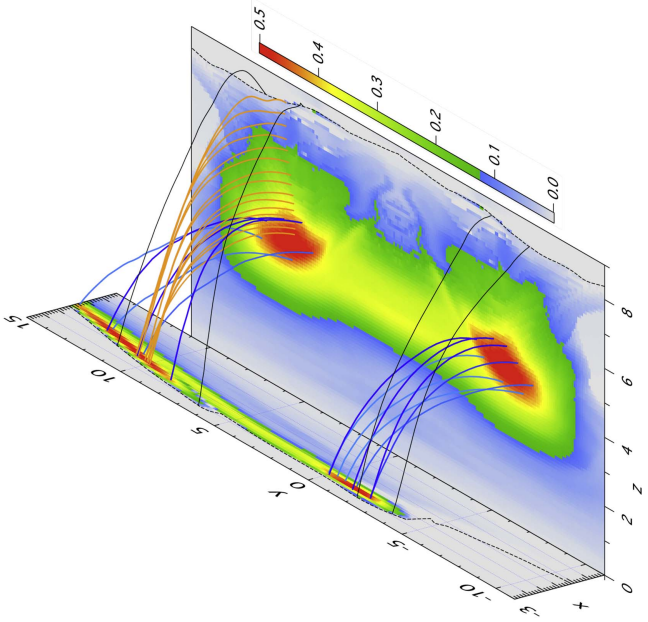

Figure 7. Perspective view of the regions enhanced particle fluxes obtained at $t = 110$ for the high-shear case, for $\xi = 0.02$, and for $v = 1$ (5.2 keV) with $\alpha = 5°$ both at $z = 0$ and $x = 0$. The color scale shows the energy gain. The blue lines are field lines connecting the regions of the enhanced fluxes, and solid black lines are separatrix field lines. The orange line shows a sample orbit of an electron contributing to the enhanced fluxes. The black dashed lines indicate the separatrices at $x = 0$ and $z = 0$.

field lines connecting the regions of the enhanced flux; the dashed black lines show the separatrices. The major difference from the case in Figure 7 is that the fluxes in Figure 8 are evaluated for 90° pitch angles at the bottom ($z = 0.5$ and $z = 0.1$, respectively), and 45° pitch angles for the medium-shear case and 25° pitch angles at $x = 0$ for the low-shear case. These pitch angles roughly correspond to mirroring orbits at the bottom in the region of the largest flux increase.

Figure 8(b) also shows a narrow region of the enhanced flux below the main region. Such an enhancement is somewhat less pronounced in Figure 8(a). This is related to particles on flux tubes that collapse downward and become compressed in front of the main region, which consists of reconnected field lines.

8. Sources

To identify the properties at the sources of the orbits contributing to the enhanced fluxes, we have chosen typical locations within the enhanced flux regions, as illustrated in Figures 7 and 8, and traced the phase space trajectories backward for a full velocity distribution. Figure 9 provides an overview of those properties, panels (a)–(d) are for the high-shear, initially force-free case, and panels (e)–(h) are for the medium-shear case. The locations and times chosen are $x = 0$, $y = 5.4$, $z = 4.5$, $t = 110$ for the high-shear case, and $x = y = 0$, $z = 3.5$, $t = 105$ for the medium-shear case. These locations were chosen to be in the center of the regions of the enhanced fluxes (the red blobs in the vertical cuts in Figures 7 and 8(a)). In both cases, we have chosen the parameter set in Equation (2) with $\xi = 0.02$, such that $u = 1$ corresponds to an energy of ~5 keV. The top panels (a) and (e) of Figure 7 show the velocity distributions, including the field-aligned parts, assuming Maxwellian source distributions with $kT_0 = 0.04$ (0.2 keV). The color corresponds to the logarithm of the phase space density. The dashed lines indicate the loss cones calculated at the chosen locations and times. It is wider in the high-shear case, not only because of the larger shear but also because of the asymmetry between the magnetic fields at the footpoints; the loss cone is determined by the weaker of the two (see Grady et al. 2012).

The loss cone increases as the field strength at the loop top increases during the collapse. There is hence a population of particles outside the initial loss cone that gain some energy but escape before the end of the collapse (Eradat Oskoui et al. 2014). Here, we have only considered sources of particles outside the final loss cone. This is illustrated in Figures 9(b), (f). The color now represents the relative energy gain $\Delta W/W_0$. It is obvious that all particles contributing to the velocity distributions have gained energy by amounts varying between about 30% and 60% for the high-shear case and 50%–90% for the medium-shear case. The energy gain in Figures 9(b), (f) shows a weak dependence on the pitch angle but little dependence on energy, demonstrating the quasi-adiabatic acceleration.

Figures 9(c), (g) show, in the same color-coding, the velocities at the source locations, which are given in Figures 9(d), (h) below. It is obvious that the source velocities occupy a much smaller volume in velocity space than the final velocities. In contrast, the source locations show a large extent in z with a much narrower extent in x. All orbits have been traced back to the boundaries in y. It is noteworthy that, according to our assumption of Liouville's theorem, the phase space density remains conserved along a phase space trajectory. Therefore, an expansion in velocity space volume between source and final necessarily implies a contraction in real space. This is important when considering the "number problem" of particle acceleration. The constraints on acceleration mechanisms become less severe when the source population of accelerated particles comes from a significantly larger source region in space.

A comparison between Figures 9(c) and (g) with Figures 9(b) and (f) also shows that the energy gain is in the perpendicular velocity components, while the parallel components become reduced. This clearly demonstrates the dominance of the betatron effect in the acceleration of the population outside of the loss cone.

Another view at the phase space distributions is provided by Figure 10, which shows, for the medium-shear case, the source distributions (dashed lines) and the distributions after the collapse for different pitch angles (colored lines), assuming either a kappa source distribution with $\kappa = 4.5$ (Figure 10(a)) or a Maxwellian source (Figure 10(b)). For completeness, we have also included nearly field-aligned cuts (blue lines), although they would be subject to losses at the boundary. It is quite obvious that the shape of the initial distribution is conserved, as either Maxwellian or kappa, as expected from adiabatic heating (Bogachev & Somov 2007). Perhaps, due to the lack of significant Fermi acceleration and the exclusion of loss mechanisms, we did not find the formation of a power-law spectrum from a thermal source inferred by Bogachev & Somov (2007).

9. Discussion

One of the most critical issues in our simulations is the boundary condition at $z = 0$. If the imposed ideal reflection was correct, particles would not deposit energy at the

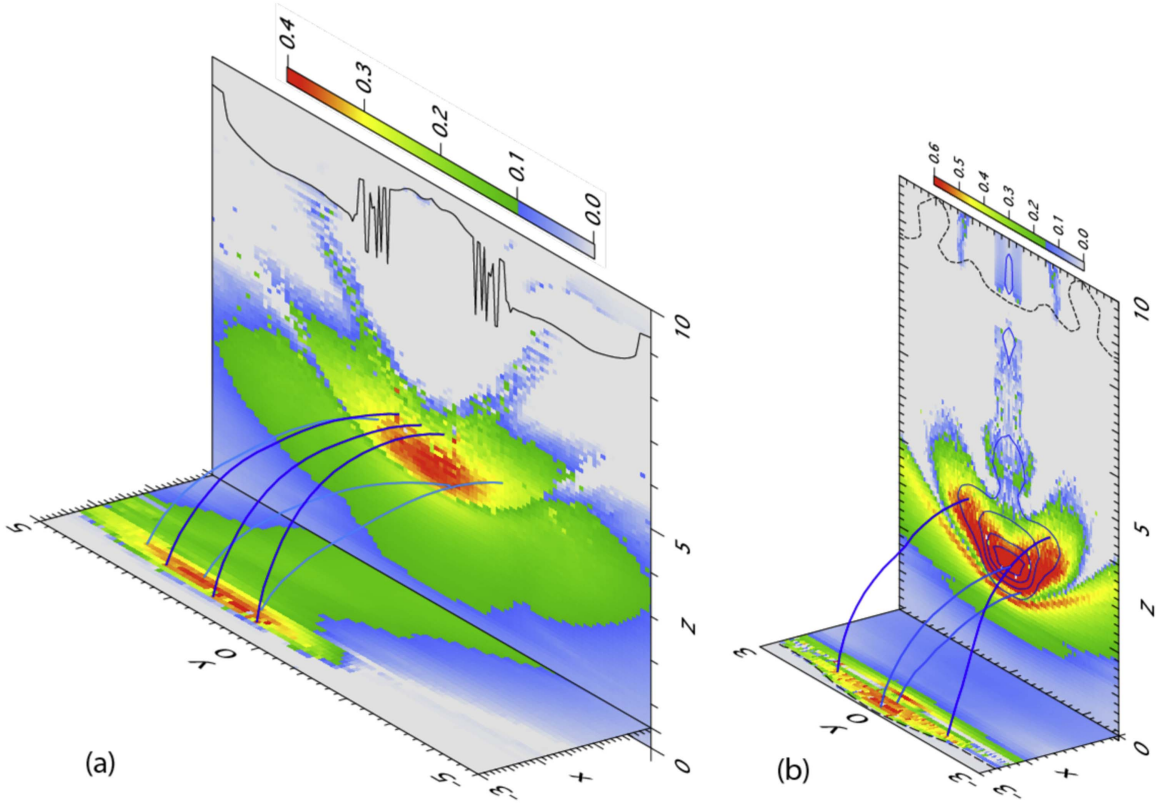

Figure 8. Perspective views of the regions of the enhanced particle fluxes (the color showing the energy gain) obtained (a) at $t = 105$ for the medium-shear case, for $\xi = 0.51$, and $u = 1$ (117 keV); and (b) for the low-shear case at $t = 130$, for $\xi = 0.02$, and $u = 1$ (5.2 keV). The bottom parts correspond to $\alpha = 90°$ and the vertical parts ($x = 0$) to $\alpha = 45°$ for the medium-shear case, and $\alpha = 25°$ for the low-shear case. The blue lines are field lines connecting the regions of the enhanced fluxes. The black dashed lines are separatrices.

footpoints. It seems more realistic to assume that all particles that hit the boundary become lost. This has interesting implications. Field-aligned particles would be lost prior to the acceleration. As the field strength increases at the loop tops from the beginning of the collapse to the stagnation, the loss cone gradually becomes wider and more particles are lost through the impact at the bottom (Eradat Oskoui et al. 2014). This effect is more significant for the medium-shear and low-shear cases, where we found increases from about 20° at the beginning collapse to about 50° and 40°, respectively, at the end of the collapse. In the high-shear case, the initial loss cone is already relatively wide, (i.e., ∼45°) due to the large guide field, increasing to ∼60°. Eventually, the population of accelerated particles becomes reduced to those outside the final loss cone in Figures 9(a) and (e). These particles could constitute a trapped loop-top population. As we saw from Figure 4, the mirror points of the particles trapped in the collapsing field move successively lower in altitude. Accelerated particles that eventually hit the bottom boundary should do so at pitch angles close to 90°. Also, since the magnetic field strengths at the two footpoints of the collapsing field lines are generally not identical (see Grady et al. 2012), the impact should be one-sided (but the same for ions and electrons).

In general, the geometry of the magnetic field plays the crucial role in the acceleration. In particular, the ratio between the loop-top magnetic field strength between the end and the beginning of a collapse determines the possible energy gain (e.g., Bogachev & Somov 2005), as is obvious for the betatron acceleration, and the ratio between the footpoint and loop-top magnetic fields determines the loss cone and thereby also limits the population that gains energy through the Fermi acceleration (e.g., Eradat Oskoui et al. 2014). In models without a guide field (e.g., Karlicky & Barta 2007; Grady & Neukirch 2009; Grady et al. 2012; Eradat Oskoui & Neukirch 2014; Eradat Oskoui et al. 2014; Borissov et al. 2016), this ratio tends to be overestimated. Three-dimensional MHD simulations, which include all field components (e.g., Kusano 2002; Török & Kliem 2005; Ugai 2007; Amari et al. 2010; Török et al. 2013; Amari et al. 2014), have focused on the eruption mechanism, rather than on the field collapse. In our simulations, both of theses ratios were rather modest, so that the energy increase was typically no larger than a factor of 2.

We should point out that even in the two-dimensional models, which found that particle energy increases by up to factor of ∼50 (Grady et al. 2012), the more typical energy increase for the 98.5% bulk of the population was less than a factor of 10. Therefore, an already pre-energized source population of 5–6 keV (Grady & Neukirch 2009; Grady et al. 2012) or even 35 keV (Karlicky & Barta 2007) was typically assumed to produce a higher-energy accelerated population.

Our particle tracing contained an additional feature, missing from most trap investigations, which is the entry of the particles into the trap. As illustrated by Figure 4, for large pitch angles, this entry could include a phase in which particles were temporarily trapped in the entry zone and the lost energy, according to the betatron effect in the decreasing field strength, before entering the collapsing trap and gaining energy again. This effect limited the energy gain even in the low-shear case,

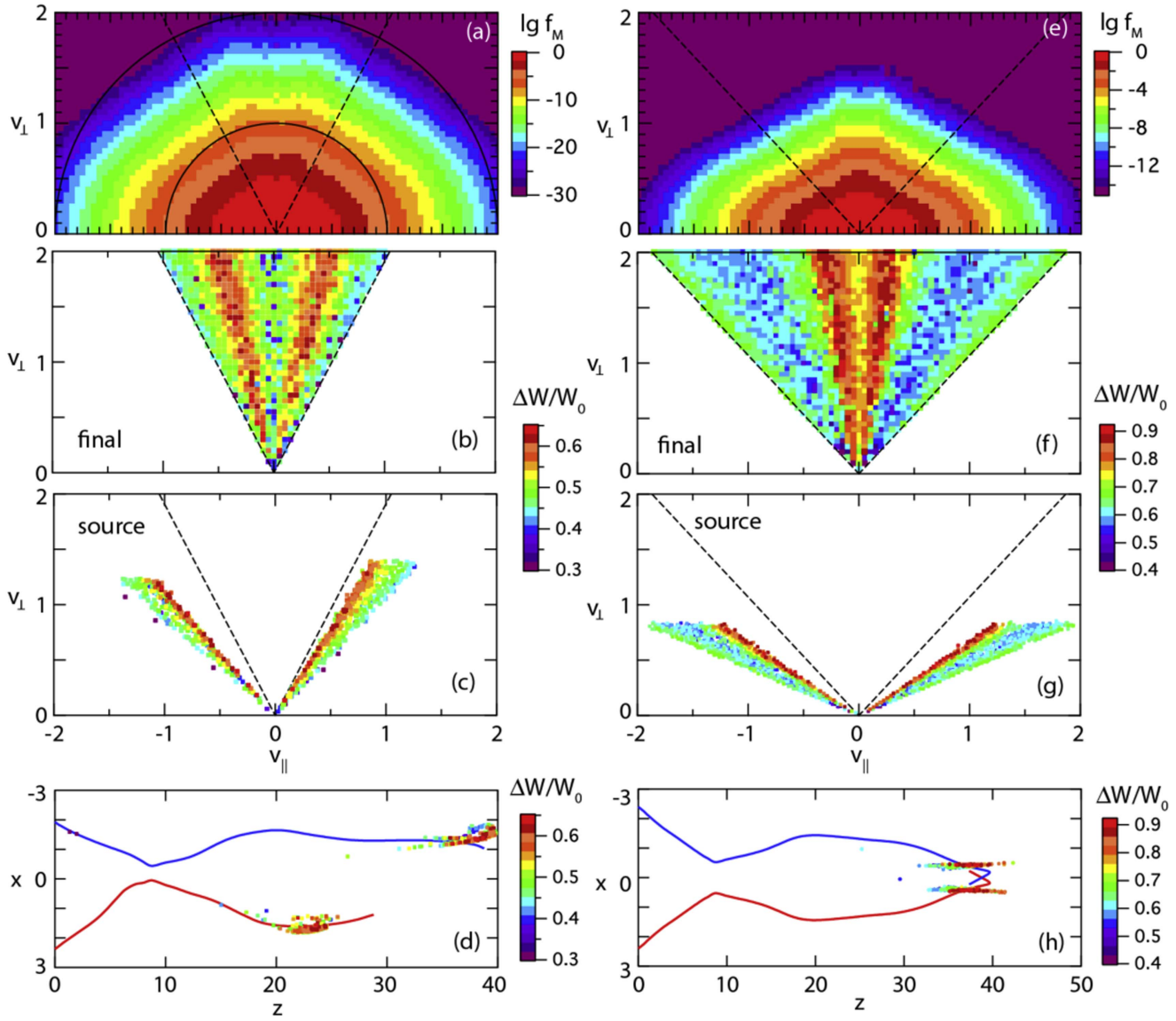

Figure 9. Velocity distributions and source properties of the enhanced fluxes. Panels (a)–(d) are for the high-shear case at $(x, y, z, t) = (0, 5.4, 4.5, 110)$; panels (e)–(h) are for the medium-shear case at $(x, y, z, t) = (0, 0, 3.5, 105)$, respectively. Panels (a) and (e) show velocity distributions; panels (b) and (f) show the relative energy gain $\Delta W/W_0$ of particles outside of the loss cone; panels (c) and (g) show the velocities at the source locations, which are color-coded by $\Delta W/W_0$; and panels (d) and (h) show the source locations in x and z, which are also color-coded by $\Delta W/W_0$, together with two sample field lines.

which is otherwise closer to the two-dimensional models investigated most often.

In another simplification, we have disregarded losses from the Coulomb collisions. According to Bogachev & Somov (2009), their affects are weak when the collapse times t_c are less that $\sim$10 s, but become appreciable for $t_c > 100$ s. In our model, the collapse time for orbits, such as illustrated in Figure 4, is about 10 dimensionless units, that is, 20 s for the parameter set in Equation (1) and 100 s for the parameter set in Equation (2). Thus, in the less relativistic case, one might expect energy losses, which reduce the fluxes primarily below $\sim$100 keV (Bogachev & Somov 2009). This mechanism, as well as other loss mechanisms, would harden the spectrum (e.g., Kontar et al. 2014) and could thus change the spectral shape toward a more kappa–like distribution (e.g., Oka et al. 2015).

A further simplification was the neglect of the parallel electric field. An estimate of the spatial extent of parallel electric field across the magnetic field indicates that, in the standard model with a single x-line or separator, only relatively few particles can be expected to approach the separator to within an ion inertial length and experience field-aligned acceleration from $E_\parallel$. For investigating and isolating the effects of the collapsing trap, it therefore seemed better to ignore $E_\parallel$, since the parallel electric field in the MHD simulation was distributed over an unrealistically wide region, To explore this matter further, we have also done some studies in which $E_\parallel$ was artificially confined to a strip of $\sim$100 km width around the x-line or separator, which is still considerably wider than the estimated ion inertial or the Spitzer resistive scale, but less than the estimated $\boldsymbol{E} \times \boldsymbol{B}$ drift during a bounce. Even in that case, we found no significant difference in the location and relative energy gain of the accelerated electrons from the case without $E_\parallel$.

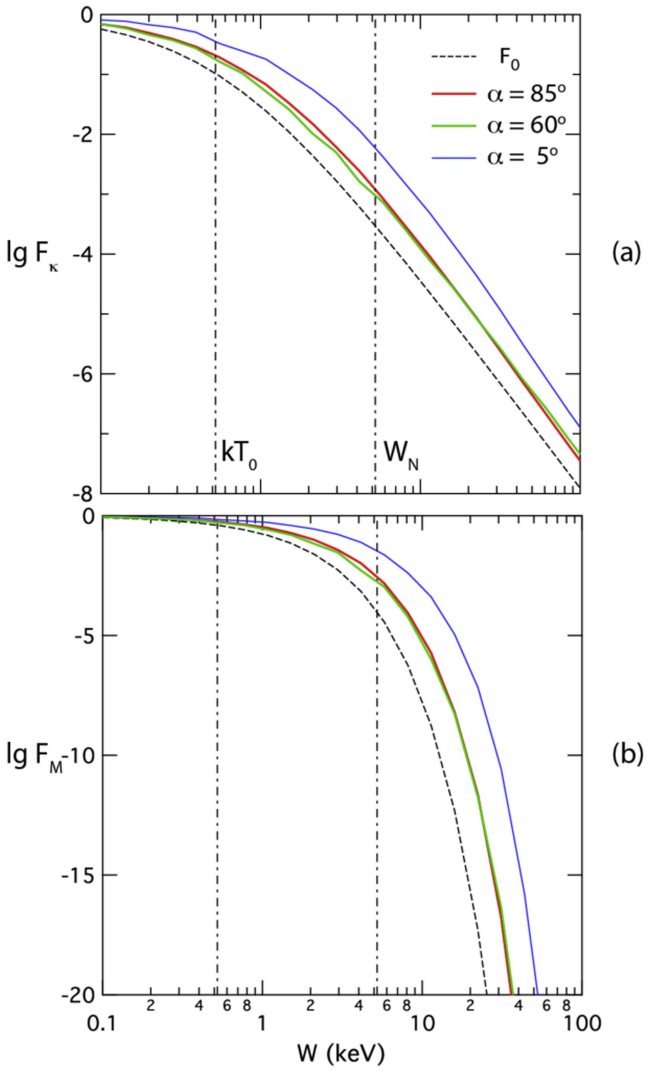

Figure 10. Phase space distributions for different pitch angles for the medium-shear case at $(x, y, z, t) = (0, 0, 3.5, 105)$ using the parameter set in Equation (2) with $\xi = 0.02$, assuming (a) a kappa source distribution and (b) a Maxwellian source. The dashed lines show the source distributions, and the colored lines show the distribution at $t = 105$ for different pitch angles α, as indicated. The dashed–dotted lines indicate the source temperature and the normalization energy W_N.

10. Summary and Conclusions

We used test particle tracing within three-dimensional MHD simulations, which are applicable to the standard flare reconnection scenario, to investigate the effects of the collapsing fields ("collapsing magnetic trap") below a reconnection site on the acceleration of electrons. In particular, we studied three cases that differed by the amount of the shear of the magnetic fields, which is related to the magnitude of the "guide" field along the main current direction at the reconnection site. The three cases ranged from a strongly sheared, initially force-free field with a very strong guide field to a low-shear field with negligible guide field, and included an intermediate case.

In all cases, we found particle acceleration within the collapsing fields. Disregarding losses at the bottom (the "photospheric" or "chromospheric" boundary), as well as other loss mechanisms, we found the acceleration to be akin to adiabatic heating, affecting particles at different energies by approximately the same factor. This factor was larger for small pitch angles. However, those particles were assumed to be reflected at the bottom boundary without a loss. Alternatively, if we consider that those particles were lost at impact, only the electrons with pitch angles around 90° outside of the loss cone would be effectively trapped and accelerated, which was predominantly caused by the betatron effect. The energy gain hence was determined by the ratio between the magnetic fields at the top of the trap before and after the collapse. This ratio varied between about 1.5 for the strongly stretched, initially force-free field with a loss cone increasing from about 45° to ∼60° and about 3 for the weakly stretched field with a loss cone increasing from ∼20° to about 40°.

We did not find large differences between the relative energy gain for different relativistic parameters, representing the ratio between a chosen unit energy and the electron rest energy, as defined by Equation (24), so that the results are easily transferable to different parameter sets. Typically, the energy gain becomes somewhat smaller for more relativistic cases, which is consistent with conclusions of Eradat Oskoui & Neukirch (2014).

The study of individual orbits showed that during the field collapse, the mirror points of a trapped particle successively move downward and closer to the surface. Therefore, particles that eventually hit the surface and deliver their energy after acceleration should have pitch angles close to 90°. Small pitch angle particles would hit the surface early without having gained any significant energy.

The particles entering the collapsing magnetic trap and becoming affected by the acceleration were found to originate from a much wider source region, such that only a small fraction from that source becomes accelerated. This, in principle, alleviates the "number problem." However, the amount of the acceleration in our simulations was insufficient to produce a substantial high-energy tail from a regular coronal source population.

Although the collapsing trap mechanism in the present study is not a likely candidate for generating a significant power-law high-energy tail to a Maxwellian particle distribution, it can be effective in enhancing the fluxes of a seed population that already has a higher-energy power-law tail added to it. The fact that the acceleration predominantly affects the population of the large pitch angles makes it a more plausible candidate for loop-top (or above loop-top) sources. However, the population that is initially outside of the loss cone becomes energized and escapes when the loss cone widens and might contribute to footpoint sources. The effective heating in the trap could also render it a possible mechanism for flares that show prolonged heating before the impulsive phase (e.g., Veronig et al. 2002; Battaglia et al. 2014) or for a long time during the post-flare phase (e.g., Kuhar et al. 2017), which is apparently without a significant acceleration. It could also be a mechanism for flares that appear entirely thermal (e.g., Fleishman et al. 2015).

Numerical work was conducted at Los Alamos National Laboratory under the auspices of the US Department of Energy, supported by NASA through grants NNX13AD10G and NNX13AD21G, and by the National Science Foundation through grants 1203711 and 1602655. L.F. would like to acknowledge support by the UK STFC under grant ST/L000741/1. T.N. acknowledges support by the UK STFC under grant ST/N000609/1. Simulation data are available

from the first author upon request. J.B., M.B., and L.F. gratefully acknowledge the hospitality and support of the International Space Science Institute, Bern, Switzerland, and the fruitful discussions with the ISSI group on Particle Acceleration in Solar Flares and Terrestrial Substorms.

ORCID iDs

J. Birn https://orcid.org/0000-0002-1496-4076
M. Battaglia https://orcid.org/0000-0003-1438-9099
T. Neukirch https://orcid.org/0000-0002-7597-4980

References

Amari, T., Aly, J. J., Mikic, Z., & Linker, J. 2010, ApJL, 717, L26
Amari, T., Canou, A., & Aly, J. J. 2014, Natur, 514, 465
Aschwanden, M. J., Caspi, A., Cohen, C. M. S., et al. 2017, ApJ, 836, 17
Aschwanden, M. J., Holman, G., O'Flannagain, A., et al. 2016, ApJ, 832, 27
Baker, D. N., Pulkkinen, T. I., Angelopoulos, V., Baumjohann, W., & McPherron, R. L. 1996, JGR, 101, 12975
Battaglia, M., Fletcher, L., & Simões, P. J. A. 2014, ApJ, 789, 47
Birn, J., Artemyev, A. V., Baker, D. N., et al. 2012, SSRv, 173, 49
Birn, J., Fletcher, L., Hesse, M., & Neukirch, T. 2009, ApJ, 114, 1151
Birn, J., Forbes, T. G., & Hesse, M. 2006, ApJ, 645, 732
Birn, J., Hesse, M., Nakamura, R., & Zaharia, S. 2013, JGR, 118, 1960
Birn, J., Iinoya, F., Brackbill, J. U., & Hesse, M. 1996, GeoRL, 23, 323
Birn, J., Runov, A., & Hesse, M. 2014, JGR, 119, 3604
Birn, J., Thomsen, M. F., & Hesse, M. 2004, PhPl, 11, 1825
Bogachev, S. A., & Somov, B. V. 2005, AstL, 31, 537
Bogachev, S. A., & Somov, B. V. 2007, AstL, 33, 54
Bogachev, S. A., & Somov, B. V. 2009, AstL, 35, 57
Book, D. L., Boris, J. P., & Hain, K. 1975, JCoPh, 18, 248
Borissov, A., Neukirch, T., & Threlfall, J. 2016, SoPh, 291, 1385
Büchner, J., & Zelenyi, L. M. 1989, JGR, 94, 11821
Carmichael, H. 1964, NASSP, 50, 451
Drake, J. F., & Shay, M. A. 2007, in Reconnection of Magnetic Fields: MHD and Collisionless Theory and Observations, ed. J. Birn & E. R. Priest (Cambridge: Cambridge Univ. Press), 87
Emslie, A. G., Dennis, B. R., Holman, G. D., & Hudson, H. S. 2005, JGRA, 110, 11103
Emslie, A. G., Dennis, B. R., Shih, A. Y., et al. 2012, ApJ, 759, 71
Eradat Oskoui, S., & Neukirch, T. 2014, A&A, 567, A131
Eradat Oskoui, S., Neukirch, T., & Grady, K. J. 2014, A&A, 563, A73
Fleishman, G. D., Nita, G. M., & Gary, D. 2015, ApJ, 802, 122
Forbes, T. G., Malherbe, J., & Priest, E. R. 1989, SoPh, 120, 285
Forbes, T. G., & Priest, E. R. 1983, SoPh, 84, 169
Gary, G. A. 2001, SoPh, 203, 71
Giuliani, P., Neukirch, T., & Wood, P. 2005, ApJ, 635, 636
Grady, K. J., & Neukirch, T. 2009, A&A, 508, 1461
Grady, K. J., Neukirch, T., & Giuliani, P. 2012, A&A, 546, A85
Hamilton, B., Fletcher, L., McClements, K. G., & Thyagaraja, A. 2005, ApJ, 625, 496
Hannah, I. G., & Fletcher, L. 2006, SoPh, 236, 59
Hesse, M. 2007, in Reconnection of Magnetic Fields: MHD and Collisionless Theory and Observations, ed. J. Birn & E. R. Priest (Cambridge: Cambridge Univ. Press), 108
Hesse, M., & Birn, J. 1993, JGR, 98, 3973
Hirayama, T. 1974, SoPh, 34, 323
Hones, E. W., Jr. 1977, JGR, 82, 5633
Hyman, J. M. 1983, SIAM J. Sci. Stat. Comput., 4, 645
Inhester, B., Birn, J., & Hesse, M. 1992, SoPh, 138, 257
Karlicky, M., & Barta, M. 2006, ApJ, 647, 1472
Karlicky, M., & Barta, M. 2007, AdSpR, 39, 1427
Karlicky, M., & Kosugi, T. 2004, A&A, 419, 1159
Kontar, E. P., Bian, N. H., Emslie, A. G., & Vilmer, N. 2014, ApJ, 780, 176
Kopp, R. A., & Pneuman, G. W. 1976, SoPh, 50, 85
Kuhar, M., Krucker, S., Hannah, I. G., et al. 2017, ApJ, 835, 6
Kusano, K. 2002, ApJ, 571, 532
Lin, R., & Krucker, S. 2012, SSRv, 173, 49
McPherron, R., Russell, C., & Aubry, M. 1973, JGR, 78, 3131
Miller, J. A., Cargill, P. J., Emslie, A. G., et al. 1997, JGR, 102, 14631
Northrop, T. G. 1963, The Adiabatic Motion of Charged Particles (New York: Wiley)
Oka, M., Ishikawa, S., Saint-Hilaire, P., Krucker, S., & Lin, R. P. 2013, ApJ, 764, 6
Oka, M., Krucker, S., Hudson, H. S., & Saint-Hilaire, P. 2015, ApJ, 799, 129
Schindler, K., Hesse, M., & Birn, J. 1988, JGR, 93, 5547
Somov, B. V., & Kosugi, T. 1997, ApJ, 485, 859
Sturrock, P. A. 1966, Natur, 211, 695
Török, T., & Kliem, B. 2005, ApJL, 630, L97
Török, T., Temmer, M., Valori, G., et al. 2013, SoPh, 286, 453
Ugai, M. 2007, PhPl, 14, 102904
Vasyliunas, V. 1968, JGR, 73, 2839
Veronig, A., Vrsnak, B., Dennis, B. R., et al. 2002, A&A, 392, 699
Yokoyama, T., & Shibata, K. 2001, ApJ, 549, 1160